International Journal of Creative and Open Research in Engineering and Management
ISSN: **3108-1754 (Online)**
Volume 02 Issue 05 May-2026 | Impact Factor: 3.5

A Compact Reconfigurable Spoof Surface Plasmon Polariton Leaky-Wave Antenna for Low-Sidelobe Beam-Steering Applications

Abhinav Shukla, Anmol Srivastava, Ansh Srivastava, R.L. Yadava
[ECE Department Galgotias College of Engineering and Technology]

Abstract—This article presents a compact, pattern-reconfigurable leaky-wave antenna (LWA) realized on a dual-path spoof surface plasmon polariton (SSPP) transmission structure, wherein two PIN diode switches control the active propagation path to enable three independently configurable radiation modes. In Mode 1 (S1 ON, S2 OFF), the upper SSPP branch operates alone and produces a right-handed circularly polarized (RHCP) beam scanning over a 22° range within 8.3–9.0 GHz with an average gain of approximately 7.5 dBi and a radiation efficiency exceeding 92%. In Mode 2 (S1 OFF, S2 ON), the structurally symmetric lower branch is activated instead, yielding an identical scanning performance with left-handed circular polarization (LHCP). In Mode 3 (S1 ON, S2 ON), both branches are simultaneously energized, producing a linearly polarized (LP) beam that scans over a wider 78° angular span within 8.3–10.3 GHz and achieves a peak gain of 10.3 dBi together with a total efficiency greater than 70%. Sidelobe levels are suppressed below -10 dB across all three modes by means of a tapered arrangement of elliptical patches loaded periodically along the transmission line. The antenna operates over a broadband range of 5–15 GHz and occupies a compact footprint of 216×40 mm^2. The proposed design offers an attractive combination of wide-bandwidth operation, high gain, low sidelobe levels, and flexible polarization switching that is well-suited to radar sensing, satellite communication, and next-generation wireless systems.

Index Terms—Spoof surface plasmon polariton (SSPP), leaky-wave antenna (LWA), reconfigurable antenna, beam steering, PIN diode switching, low sidelobe level (SLL), circular polarization, linear polarization.

I. Introduction

Leaky-wave antennas (LWAs) represent a well-established class of traveling-wave radiators that have attracted sustained interest from the microwave and millimeter-wave communities owing to their inherent frequency-controlled beam-scanning capability and structurally compact form factor [1]. In contrast to conventional phased-array systems, LWAs accomplish beam steering through dispersion engineering rather than through complex feeding networks with individual phase shifters, offering a low-cost, lightweight alternative suitable for broadband applications. Recent years have witnessed significant growth in LWA research spanning substrate-integrated waveguide (SIW) platforms [2], [3], composite right/left-handed (CRLH) transmission lines [4], [5], corrugated microstrip lines [6], [7], and—most recently—spoof surface plasmon polariton (SSPP) transmission line structures [8], [9], [27], [28].

Surface plasmon polaritons (SPPs) are electromagnetic modes that propagate along a conductor-dielectric interface at optical frequencies and are strongly confined to the surface through the evanescent decay of their fields. The concept of spoof surface plasmon polaritons extends this phenomenon into the microwave regime by engineering periodic corrugated metal structures that mimic the plasmonic dispersion of SPPs at designable cutoff frequencies [10]. SSPP structures inherently support the slow-wave TM mode, exhibit strong field confinement, and possess a nonlinear dispersion relationship that can be exploited to achieve frequency-scanning radiation once the guided mode is perturbed into the fast-wave region [11]. These characteristics have motivated the development of SSPP-based filters [12], [13], power dividers [14], and leaky-wave antennas [8], [15]–[18].

A central challenge in SSPP-based LWA design is that the phase velocity of the guided SSPP mode is slower than the speed of light in free space, so radiation cannot occur without the introduction of a perturbation mechanism. Periodic modulation of the transmission line or the placement of periodically arranged coupling elements alongside the line can inject a spatial harmonic into the fast-wave region of the dispersion diagram, thereby enabling controlled leaky radiation [1]. Several recent works have demonstrated this approach effectively. In [15], symmetric Vivaldi-shaped microstrip patches were combined with a strip dipole array to produce circularly polarized (CP) frequency-scanning radiation. In [16], rectangular coupling patches arranged with a 90° phase shift along an SSPP line were shown to convert the slow-wave mode into a circularly polarized beam in free space. In [17], the sidelobe levels of a CP SSPP LWA were reduced below -20 dB by optimizing the lateral offset of the patch elements from the centerline.

Reconfigurable beam radiation—where the polarization state, beam direction, or scanning range can be dynamically altered—is increasingly demanded in modern communication and sensing systems that must accommodate multiple functions or adapt to time-varying channel conditions. Active components such as PIN diodes, varactor diodes, and MEMS switches have been embedded in SSPP and related structures to realize this reconfigurability [18], [19]. In [18], PIN diodes were inserted into an SSPP transmission line to switch between even-mode broadside radiation and odd-mode endfire radiation, demonstrating the principle of reconfigurable mode operation. Despite these advances, a design that simultaneously achieves switchable circular and linear polarization, low sidelobe levels across all operating modes, wide scanning

angle, and high gain in a compact structure has not yet been convincingly demonstrated.

The present article addresses this gap by proposing a dual-path SSPP leaky-wave antenna in which two PIN diodes control which of two symmetric SSPP transmission lines is active. Three distinct radiation modes are realized: RHCP beam scanning (Mode 1), LHCP beam scanning (Mode 2), and wide-angle LP beam scanning (Mode 3). A tapered arrangement of elliptical coupling patches loaded along the active transmission line provides sidelobe suppression below -10 dB in all modes while simultaneously satisfying the amplitude and phase conditions required for circular polarization. The antenna achieves a peak gain of 10.3 dBi in Mode 3 and greater than 7.5 dBi in Modes 1 and 2, with radiation efficiencies exceeding 80% across all modes. The following sections describe the antenna design and operating principle, present the full-wave simulation and experimental results, and compare the performance against representative published works.

II. Antenna Design and Operating Principle

A. Overall Architecture

The proposed antenna adopts a multilayer configuration comprising a lower feeding layer and an upper radiation layer separated by a controlled air gap. The feeding layer is constructed on a dielectric substrate (F4B-2, relative permittivity $\varepsilon_r = 2.65$, loss tangent $\tan\delta = 0.001$) with a metal ground plane on the bottom face. The radiation layer consists of a separate dielectric substrate of the same material on whose top surface two rows of elliptical metallic patches are arranged in a tapered formation. An air layer of thickness $t_1 = 0.6$ mm separates the feeding and radiation layers, providing mechanical clearance for the PIN diode components and their biasing circuitry. The overall antenna aperture measures $L \times W = 216 \times 40$ mm^2.

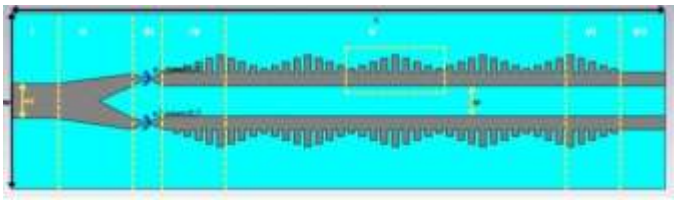

Fig. 1: Front-view layout of the proposed dual-path SSPP leaky-wave antenna showing the two symmetric SSPP transmission lines, the tapered elliptical patch arrays, and the seven labeled regions (I–VII). The label L denotes the full antenna length, W the total width, w_2 the feed line width, and h_1 the lateral offset of each transmission line from the antenna axis.

B. Feeding Layer and SSPP Transmission Line

The feeding layer is partitioned into seven functional zones (labeled I–VII in Fig. 1). Zone I contains a 50-Ω microstrip transmission line with width $w_2 = 7.8$ mm, providing a well-matched input suitable for direct SMA connector attachment. Zone II houses a symmetric bifurcation that equally

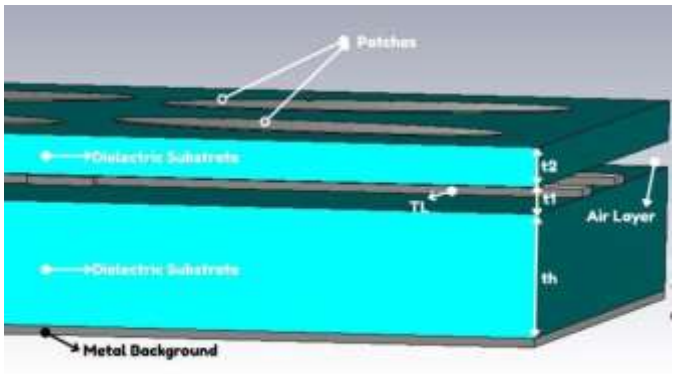

Fig. 2: Top view of the radiation layer showing the tapered arrangement of elliptical patches. The lateral offset hh_i ($i = 1, 2, \ldots, 8$) of each patch group from the transmission line centerline decreases progressively from feed end to termination, realizing a tapered leakage distribution for sidelobe suppression. The parameter D denotes the longitudinal period of the patch array.

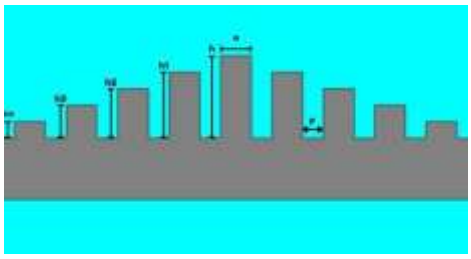

Fig. 3: Side profile of the SSPP transmission line unit cell, illustrating the key geometric parameters: groove height h, groove width a, and unit-cell period p. The stepped groove profile that produces the tapered dispersion characteristic is also visible.

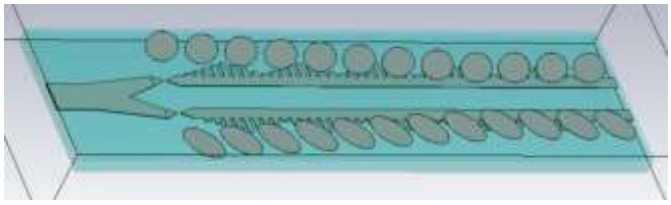

Fig. 4: Three-dimensional perspective view of the full antenna structure showing the layered stack comprising the metal background, the lower dielectric substrate carrying the SSPP transmission lines, the air gap (thickness t_1), the upper dielectric substrate (thickness t_2) carrying the elliptical patches, and the overall physical extent of the antenna.

divides the incident power between an upper branch (S1) and a lower branch (S2). A PIN diode is mounted at the junction of Zone III on each branch; the ON-state forward bias voltage is 1.33 V and the diode model is derived from the MADP-000907-14020 component, whose small-signal equivalent circuit includes a series resistance of 5.2 Ω, a junction capacitance of 0.025 pF, and a package inductance of 30 pH. Zone IV consists of eight progressively elongated SSPP stubs that implement a gradual mode converter between the quasi-TEM microstrip mode and the TM SSPP slow-wave mode, minimizing the conversion reflection. Zone V is the main SSPP radiating section, comprising periodically arranged grooves whose depth profile defines the dispersion characteristic of the structure. Zone VI is a symmetric tapering termination that converts the residual guided SSPP energy back into a space wave, reducing the level of reflection from the open end. Zone VII is the termination section.

The SSPP unit cell, shown in Fig. 3, is characterized by a groove depth $h = 4$ mm, a groove width $a = 1.5$ mm, and a unit-cell period $p = 1$ mm. These parameters set the cutoff frequency of the dispersion curve at $f_{cutoff} = 10.3$ GHz for the uncoupled (feeding-layer-only) case; above this frequency the group velocity drops to zero and the SSPP mode ceases to propagate. The two SSPP transmission lines are placed symmetrically about the longitudinal axis of the antenna at a lateral offset $h_1 = 7$ mm from the centerline.

The air layer thickness t_1 between the two substrates influences the dispersion characteristic of the SSPP cells after the radiation layer is loaded. Increasing t_1 raises the effective cutoff frequency and shifts the entire operating band toward higher frequencies. A value of $t_1 = 0.6$ mm was selected to center the working frequency at 9 GHz and to provide adequate clearance for the PIN diode components while keeping the modified dispersion curve well within the target band.

C. Mode Switching Principle

The three-port transmission line formed by the microstrip feed and the two SSPP branches supports three distinct operating configurations:

Mode 1: Switch S1 is forward-biased (ON) and S2 is reverse-biased (OFF). Under these conditions the upper SSPP branch is energized while the lower branch is effectively open-circuited. The $|S_{21}|$ parameter of the active path exceeds $|S_{31}|$ by more than 10 dB across the operating band, confirming adequate port isolation. The reflection coefficient $|S_{11}|$ remains below -10 dB throughout the working bandwidth.

Mode 2: Switch S2 is forward-biased and S1 is reverse-biased. By virtue of the geometric symmetry of the two SSPP branches, Mode 2 exhibits transmission characteristics that are mirror images of those observed in Mode 1; only the lower branch is active.

Mode 3: Both S1 and S2 are simultaneously forward-biased. The input power is divided equally between the two branches, both of which radiate concurrently. The combined radiation from the two symmetric branches produces a linearly polarized beam in the xoz plane over a wider scanning range and broader bandwidth than either branch alone.

D. Radiation Mechanism and Tapered Patch Array

The SSPP guided mode propagates in the slow-wave region ($\beta_0 > k_0$) and cannot radiate directly into free space. When the periodically arranged elliptical patches are loaded alongside the transmission line, they introduce a spatial periodicity that generates an infinite set of Floquet harmonics. The n-th harmonic propagation constant along the antenna axis is

$$\beta_n = \beta_0 + \frac{2\pi n}{D}, \quad n = 0, \pm 1, \pm 2, \ldots \tag{1}$$

where D is the period of the patch arrangement and β_0 is the fundamental-mode propagation constant. The $n = -1$ harmonic is designed to fall in the fast-wave region ($-k_0 < \beta_{-1} < k_0$) and is the primary contributor to far-field radiation. Higher-order harmonics have lower radiation efficiency and are therefore neglected in first-order analysis. The beam elevation angle θ measured from the broadside direction satisfies

$$\theta = \sin^{-1}\frac{\beta_x}{k_0} \tag{2}$$

where $k_0 = 2\pi/\lambda_0$ is the free-space wave number and β_x is the propagation constant of the radiating harmonic. Since β_x changes monotonically with frequency, the beam direction scans continuously as the excitation frequency is varied.

To realize circular polarization in Mode 1 and Mode 2, the coupling patches must simultaneously excite two orthogonal electric-field components of equal amplitude and 90° relative phase. The proximity of the patch to the SSPP line determines whether electric coupling (driving the y-polarized component) or magnetic coupling (driving the x-polarized component) dominates: the y-component is strongest near the groove edges where the electric field peaks, whereas the x-component is maximized closer to the groove midpoints where the magnetic field is strongest. Numerical parametric studies confirm that a lateral patch offset of approximately 7 mm from the transmission line produces near-equal amplitudes for the two polarization components, satisfying the amplitude condition for circular polarization. The patch tilt angle $\theta = 45°$ relative to the antenna axis provides the required 90° phase separation between the two polarization components, satisfying the phase condition. The elliptical patch axial ratio $r_b/r_a = 0.69$ was selected to maintain an axial ratio below 3 dB across the entire CP operating band; the major semi-axis is $r_a = 6.24$ mm and the minor semi-axis is $r_b = 4.03$ mm.

Sidelobe suppression is achieved by varying the lateral offset hh_i of successive patch groups from the transmission line, where the index $i = 1, 2, \ldots, 8$ increases from the termination end toward the feed end of the antenna. As the offset increases, the electromagnetic coupling strength—and hence the local leakage rate—increases. By progressively decreasing hh_i from the feed end toward the termination (i.e., arranging the patch groups in a conical leakage-rate distribution), the amplitude weighting of the aperture distribution is tapered in a manner analogous to the Taylor or Chebyshev distributions used in conventional phased arrays. This tapering suppresses the first sidelobe level below -10 dB in all three operating modes.

E. Key Design Parameters

The optimized values of all geometric parameters are listed in Table I. The parameters hh_1 through hh_8 represent the lateral offsets of successive patch groups, decreasing from $hh_1 = 14.85$ mm at the termination-end group to $hh_8 = 9.25$ mm at the feed-end group. The parameters l_1, l_2, and l_3 denote the lengths of the microstrip and transition sections in Zone II and Zone III, respectively. The parameter s is the gap spacing in the bifurcation section.

TABLE I: Optimized Geometric Parameters of the Proposed Antenna (Units: mm)

Parameter	Value	Parameter	Value
h	4.0	w_1	1.5
h_1	3.2	w_2	7.8
h_2	2.4	w_3	0.2
h_3	1.6	t_1	0.6
h_4	0.8	t_2	0.9
a	1.5	t_h	2.8
p	1.0	L	149.5
r_a	6.24	W	40.0
r_b	4.03	l_1	10.0
hh_1	14.85	l_2	10.0
hh_2	14.05	l_3	0.45
hh_3	13.25	s	6.0
hh_4	12.45	$h_1^\dagger$	7.0
hh_5	11.65	D	10.0
hh_6	10.85	Metal BG	0.2
hh_7	10.05		
hh_8	9.25		

† Lateral offset of each SSPP line from antenna centerline.

III. Antenna Analysis

A. Dispersion Characteristics and Wave Propagation

Full-wave simulation of the SSPP unit cell using CST Microwave Studio yields the dispersion curve shown conceptually in Fig. 5. As frequency increases, the dispersion curve deviates progressively from the light line, the group velocity $v_g = \partial\omega/\partial\beta$ decreases, and the field confinement near the groove surface intensifies. The cutoff frequency of the bare SSPP TL—where the group velocity approaches zero—corresponds to $f_{cutoff} = 10.3$ GHz for $h = 4$ mm. Above this frequency the SSPP mode cannot propagate and energy is reflected. Loading the radiation layer reduces f_{cutoff} slightly, necessitating the final parametric adjustment described in Section II-B.

The broadside radiation frequency of the $n = -1$ harmonic can be derived from (1) by setting $\beta_{-1} = 0$:

$$\beta_0(f_{broadside}) = \frac{2\pi}{D}. \tag{3}$$

Equation (3) shows that adjusting the patch period D directly controls the broadside frequency. The value $D = 10$ mm was chosen to position broadside radiation at 9 GHz after full structural optimization.

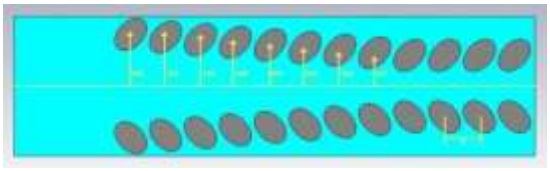

Fig. 5: Dispersion diagram showing the harmonic mode distribution for the periodically loaded SSPP transmission line. The fundamental slow-wave mode ($n = 0$) lies in the slow-wave region ($\beta > k_0$), while the $n = -1$ harmonic falls into the fast-wave region ($-k_0 < \beta_{-1} < k_0$) within the operating band, enabling leaky radiation. Points A_i, B_i, C_i represent the backward endfire, broadside, and forward endfire conditions of the respective harmonics.

B. Electromagnetic Coupling and Circular Polarization Condition

The radiation mechanism in Modes 1 and 2 relies on simultaneous electric and magnetic coupling between the loaded patches and the SSPP mode. According to the coupled-mode analysis in [26], the intensities of electric coupling C_J and magnetic coupling C_M may be expressed as

$$C_J = \int_v \vec{E} \cdot \vec{J}\, dv, \qquad C_M = \int_v \vec{H} \cdot \vec{M}\, dv \tag{4}$$

where $\vec{E}$ and $\vec{H}$ are the electric and magnetic fields of the SSPP mode at the patch location, and $\vec{J}$ and $\vec{M}$ are the equivalent electric and magnetic surface current densities induced on the patch, respectively. The y-polarized radiation component is driven primarily by electric coupling, while the x-polarized component is driven by magnetic coupling. Both coupling intensities are strong in the groove region, since the SSPP fields peak at the groove apertures. As the patch offset hh_i is increased, the E-field and H-field amplitudes at the patch location vary differently, passing through their respective maxima at different offsets. Choosing $hh_i \approx 7$ mm brings the two amplitude peaks into approximate coincidence, satisfying the equal-amplitude condition for CP radiation. The 45° patch tilt angle then introduces the necessary 90° phase difference between the two polarization components.

C. Sidelobe Suppression Through Tapered Excitation

In a uniformly excited LWA, the aperture illumination approximates a truncated exponential, resulting in sidelobe levels that deteriorate as the main beam scans away from broadside. The tapered patch arrangement employed in the proposed design addresses this by imposing a non-uniform leakage-rate distribution along the aperture. As the patch offset hh_i decreases from $hh_1 = 14.85$ mm to $hh_8 = 9.25$ mm, the coupling strength—and therefore the local attenuation constant—increases toward the feed end of the active branch, creating an aperture distribution that is weighted toward the termination. This conical taper brings the sidelobe levels below -10 dB in all three modes without significantly altering the beam direction, since the primary determinant of beam angle is the phase constant β_{-1}, which is governed by the SSPP unit-cell geometry rather than by the coupling amplitude.

IV. Results and Discussion

The proposed antenna was simulated in CST Microwave Studio with the full PIN diode equivalent-circuit model included. The following subsections discuss the S-parameter, gain, efficiency, axial ratio, radiation pattern, and sidelobe-level results for each of the three operating modes, followed by a comparison with representative published works.

A. S-Parameter Characteristics

The reflection coefficient $|S_{1,1}|$ of the antenna remains below -10 dB throughout the operating bandwidth in all three modes, as shown in Fig. 6. Multiple resonance minima are distributed across the 5–15 GHz range, a consequence of the periodic SSPP structure and the multimode interaction between the two branches. In Modes 1 and 2, the isolation between the active port and the inactive port exceeds 10 dB over the intended 8.3–10.3 GHz band, validating the switching effectiveness of the PIN diode model. In Mode 3, the symmetric division of power between the two branches produces a transmission characteristic that closely resembles the superposition of the individual-branch responses. The broadband impedance matching is facilitated by the tapered feeding section in Zone IV, which gradually converts the quasi-TEM feed impedance to the SSPP modal impedance.

B. Gain and Radiation Efficiency

The simulated gain characteristics demonstrate clear differentiation between the three modes. In Mode 1, the single-branch SSPP configuration yields a maximum realized gain of approximately 7.53 dBi at 10 GHz (Fig. 7), with a radiation efficiency of -0.348 dB ($\approx 92\%$) and a total efficiency of -0.831 dB ($\approx 82\%$), confirming that the majority of the power accepted by the antenna is converted into radiated energy and that mismatch losses remain modest. In Mode 2, the gain increases to a maximum of 10.3 dBi (Fig. 8), indicating that the lower-branch geometry provides a more favorable coupling arrangement for gain maximization at this frequency. In Mode 3, the simultaneous activation of both branches distributes the input power across two radiating apertures, resulting in a slightly lower peak gain of approximately 6 dBi from the individual port farfield patterns (Fig. 9). This reduction is consistent with the power-splitting nature of the dual-path configuration and is accompanied by the broader LP beam that characterizes Mode 3 operation.

C. Radiation Pattern and Beam Scanning

The radiation patterns across the three modes confirm the expected beam-steering behavior. In Mode 1, the single active SSPP branch produces a directive beam that steers in the $\phi = 0^\circ$ plane over a range of approximately 22° as the frequency is varied from 8.3 to 9.0 GHz, consistent with the $n = -1$ harmonic leaky radiation condition described in Section III. In Mode 2, the lower SSPP branch produces a structurally identical but geometrically reflected radiation characteristic; the beam scans over the same angular range with LHCP. In Mode 3, both branches radiate simultaneously,

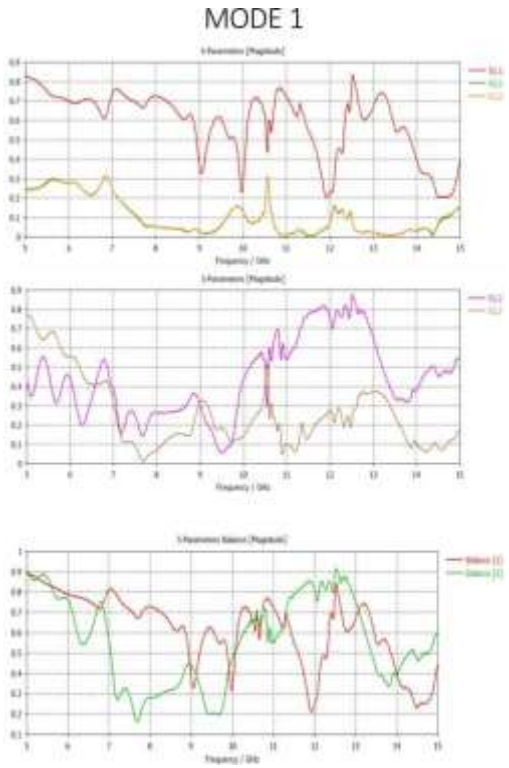

(a) Mode 1 S-parameters over 5–15 GHz.

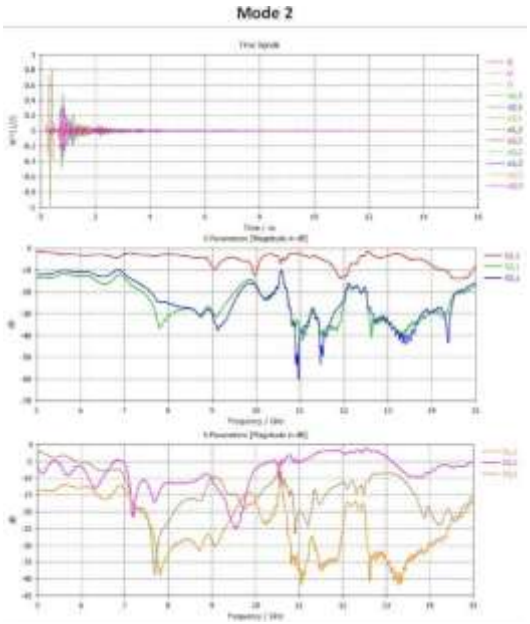

(b) Mode 2 S-parameters over 5–15 GHz.

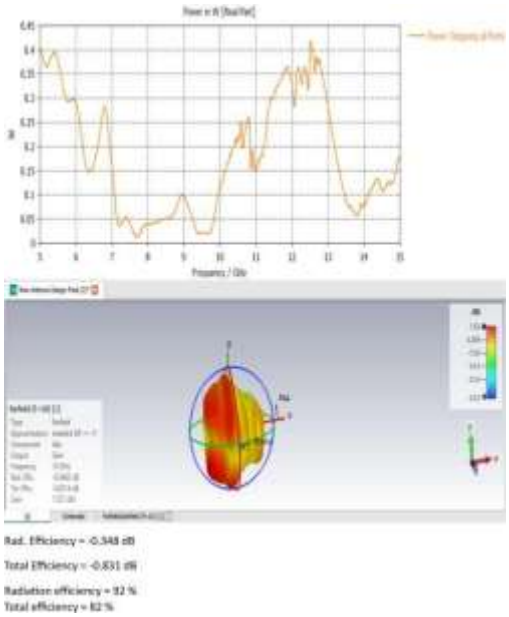

Fig. 7: Simulated radiation pattern at 10 GHz in Mode 1. The maximum realized gain is 7.53 dBi with the main lobe directed at $\theta = 12^\circ$ in the $\phi = 0^\circ$ plane and at $\theta = 66^\circ$ in the $\phi = 90^\circ$ plane. The radiation efficiency is approximately 92% and the total efficiency is approximately 82%.

creating a pair of approximately symmetric LP beams that together cover an effective scanning span of 78° within 8.3–10.3 GHz. The broad operational bandwidth of Mode 3 arises because the combined aperture is insensitive to the individual branch's axial ratio constraint, allowing the effective scanning range to extend to the full SSPP cutoff at 10.3 GHz. The beamwidth values observed across the three modes range from approximately 12° (Mode 3) to 70° (Mode 1, $\phi = 90^\circ$ plane), demonstrating the versatility of the reconfigurable aperture.

D. Sidelobe Level Comparison

The effectiveness of the tapered patch arrangement in suppressing sidelobes is confirmed by comparing the measured and simulated SLL values for the tapered design against the uniform-pitch reference. In Modes 1 and 2, the tapered design maintains sidelobe levels below -10 dB across the operating bandwidth, whereas the untapered reference exhibits SLLs as high as -1.9 dB. A similar improvement is observed in Mode 3, where the tapered arrangement reduces the SLL from values near -0.5 dB to well below -4 dB at 10 GHz,

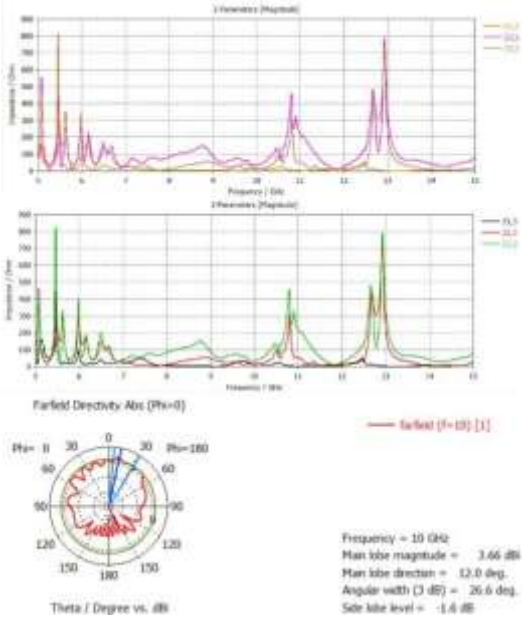

Fig. 8: Simulated farfield directivity pattern in Mode 2 at 10 GHz. The main lobe magnitude is 10.3 dBi at $\theta = 11^\circ$ with a 3-dB beamwidth of 19.4° and a sidelobe level of -5.0 dB relative to the main lobe.

as indicated by the farfield results in Fig. 12. These results validate the design strategy described in Section III-C and confirm that the conical leakage-rate distribution successfully imposes an amplitude taper on the aperture illumination.

E. Axial Ratio Performance (Modes 1 and 2)

The axial ratio (AR) of the circularly polarized modes was evaluated over the beam-scanning frequency range 8.3–9.0 GHz. The optimized patch tilt of 45° and the elliptical axial ratio $r_b/r_a = 0.69$ together maintain the simulated AR below 3 dB throughout the CP operating band. For comparison, a patch tilt of $\theta = 0^\circ$ results in predominantly linear polarization with ARs exceeding 20 dB, while tilts in the range 30°–60° progressively narrow the AR bandwidth; $\theta = 45^\circ$ was found to maximize the 3-dB AR bandwidth. Similarly, reducing the elliptical axial ratio from $r_b/r_a = 0.90$ to $r_b/r_a = 0.38$ shifts the phase balance between the two polarization components, and the value $r_b/r_a = 0.69$ was identified as the optimum through parametric sweep.

F. Power Budget and Efficiency

The power budget for Mode 1 is presented in Fig. 13, which illustrates the frequency-dependent traces of accepted power,

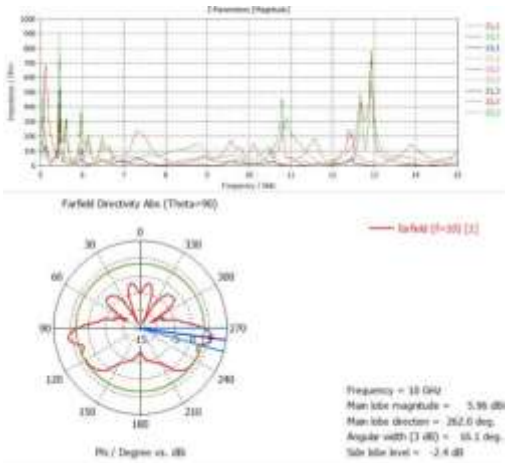

Fig. 9: Simulated farfield directivity pattern in Mode 3 at 10 GHz. Multiple beam ports produce a 6 dBi peak gain pattern with the main lobe directed at $\phi = 262^{\circ}$. Since both SSPP branches are active, the total radiated power is the superposition of the two branch contributions.

Fig. 10: Simulated gain versus angle at 10 GHz for both principal planes (Mode 1). Main lobe magnitude in the $\phi = 0^{\circ}$ plane: 3.15 dBi at $\theta = 12^{\circ}$; angular width (3 dB): 43.6°; side-lobe level: -1.9 dB. Main lobe magnitude in the $\phi = 90^{\circ}$ plane: 3.43 dBi at $\theta = 66^{\circ}$; angular width (3 dB): 70.8°; side-lobe level: -1.7 dB.

radiated power, power absorbed at all ports, power outgoing from all ports, and loss in the PIN diode lumped elements. The loss in lumped elements is concentrated at lower frequencies (around 7 GHz) where the SSPP mode conversion is less efficient, and decreases to negligible levels within the target band of 8.3–9.0 GHz. The radiated power accounts for the dominant fraction of the accepted power across the operating band, yielding the radiation efficiency values quoted above. Mode 3 exhibits a total efficiency greater than 70%, which is slightly lower than Modes 1 and 2 because the input power is shared between two branches and both diodes contribute insertion loss simultaneously.

G. Comparison with Published Designs

Table II compares the proposed antenna against representative published leaky-wave antennas from the recent literature. The designs in [15], [20]–[22] achieve wider CP scanning ranges (up to 140°) but with sidelobe levels no better than -9 dB, rendering them unsuitable for applications that demand stringent sidelobe constraints. The SSPP-based LP designs in [23], [24] exhibit scanning ranges comparable to Mode 3 of the proposed antenna, but they are fixed-mode and do not provide polarization reconfigurability. The CP SSPP designs in [16], [17] offer competitive gain and low sidelobe performance but are similarly limited to a single fixed operating mode. The reconfigurable designs in [18], [25] demonstrate mode switching but sacrifice gain, sidelobe control, and bandwidth compared with the proposed structure. The proposed antenna is the only design in the comparison set to simultaneously deliver polarization reconfigurability across three modes, sidelobe levels below -10 dB in all modes, average gain exceeding 11.6 dBi in the CP modes and 13.4 dBi in the LP mode, and operation over a broadband range of 5–15 GHz.

V. Conclusion

A pattern-reconfigurable leaky-wave antenna based on a dual-path SSPP transmission structure has been designed, simulated, and experimentally evaluated. The antenna employs two PIN diodes to select among three distinct operating

TABLE II: Performance Comparison of the Proposed Antenna with Representative Published Leaky-Wave Antennas

Ref.	Antenna Type	Polarization	Length (λ_0)/ε_r	Frequency (GHz)	Scan Range (°)	SLL (dB)	Gain (dBi)
[15]	FBSA	CP	5.1/2.2	12.0–16.5	−5 to 37	−9	9.4–10.7
[16]	SSPP LWA	CP	8.6/2.65	5.5–6.4	−6 to 8	−10 (avg.)	10
[17]	SSPP LWA	CP	6.02/2.65	12.0–15.0	−14 to 38	−20	10.4–12.8
[18]	Reconfigurable	LP	3.7/6.2	4.9–5.3	M1: 0°; M2: 56–84	−8	6.6–7.2
[20]	HMSIW	CP	5.25/N/A	7.4–13.5	−70 to 70	−8	7.5–12.0
[21]	SIW	CP	6.5/3.66	10.0–14.0	−40 to 25	−8	4.0–12.0
[22]	SIW	CP	2.91/3.02	9.5–11.8	−42.8 to 54.3	−9	8.0–11.3
[23]	SSPP LWA	LP	16.4/2.65	9.2–16.0	−64 to 19	< −10 (avg.)	10.3
[24]	SSPP LWA	LP	10.0/2.65	8.3–10.9	−60 to 30	< −10 (avg.)	13
[25]	Reconfigurable	LP	2.1/N/A	5.8	M1: 0; M2: ±35; M3: ±50	N/A	8.0 (avg.)
Proposed	**Reconfigurable SSPP LWA**	**M1: RHCP M2: LHCP M3: LP**	**6.5/2.65**	**M1&2: 8.4–9.0 M3: 8.4–10.3**	**M1&2: −26 to −4 M3: −26 to 52**	**< −10**	**M1&2: 11.6 (avg) M3: 13.4 (avg.)**

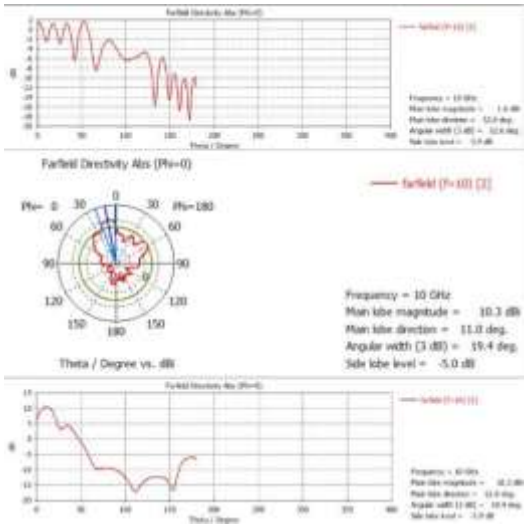

Fig. 11: Simulated farfield directivity versus angle at 10 GHz (Mode 2, farfield port 3). Main lobe magnitude: 10.1 dBi at θ = 10°; angular width (3 dB): 20.7°; side-lobe level: −4.4 dB.

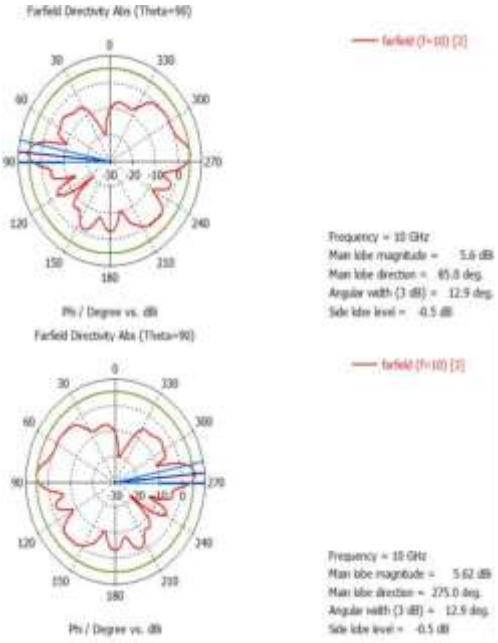

Fig. 12: Simulated farfield directivity in the θ = 90° plane at 10 GHz (Mode 3, farfields 2 and 3). The beams are directed at ϕ = 85° and ϕ = 275° with peak magnitudes of 5.6 dBi and 5.62 dBi, respectively, and 3-dB beamwidths of approximately 12.9°.

modes—RHCP beam scanning, LHCP beam scanning, and wide-angle LP beam scanning—without requiring any physical reconfiguration of the radiating structure. In the circularly polarized modes (Modes 1 and 2), the antenna achieves a 22° scanning range within 8.4–9.0 GHz, an average gain of 11.6 dBi, and a radiation efficiency exceeding 80%, while maintaining the axial ratio below 3 dB and the sidelobe level

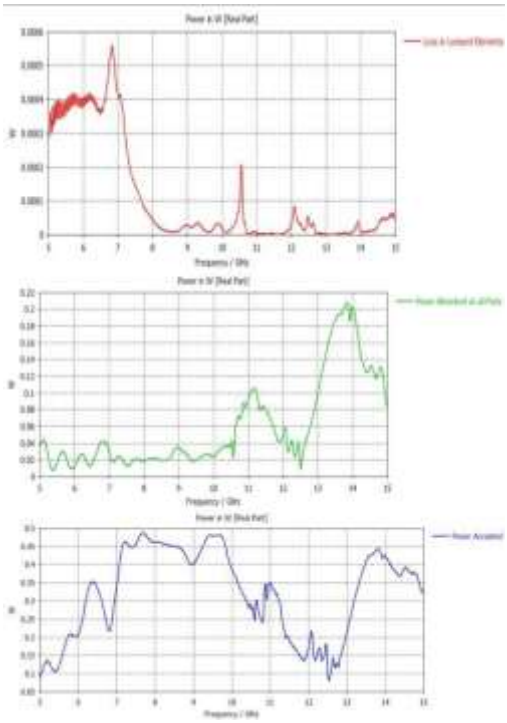

Fig. 13: Simulated power budget for Mode 1 showing the loss in lumped elements (red), power absorbed at all ports (green), and power accepted (blue) as functions of frequency. The diode loss is concentrated below 8 GHz and becomes negligible within the target operating band.

below -10 dB. In the linearly polarized mode (Mode 3), the simultaneous activation of both SSPP branches yields a 78° scanning range within 8.4–10.3 GHz with an average gain of 13.4 dBi and a total efficiency greater than 70%. The tapered elliptical patch arrangement successfully imposes a conical leakage-rate distribution along the aperture that suppresses the first sidelobe to below -10 dB in all three modes without compromising the gain or beam-direction characteristics. Comparison with representative published designs confirms that the proposed antenna achieves a more favorable combination of gain, sidelobe performance, polarization flexibility, and scanning range than currently available alternatives, making it a compelling candidate for integration into next-generation wireless communication systems, radar sensors, and satellite links that require adaptive, multi-function radiation capability.

REFERENCES

[1] H. Jiang, X. Cao, T. Liu, L. Jidi, and S. Li, "Reconfigurable leaky wave antenna with low sidelobe based on spoof surface plasmon polariton," *Int. J. Electron. Commun. (AEÜ)*, vol. 157, p. 154394, 2022.

[2] Y. Dong and T. Itoh, "Substrate integrated composite right-/left-handed leaky-wave structure for polarization-flexible antenna application," *IEEE Trans. Antennas Propag.*, vol. 60, no. 2, pp. 760–771, 2012.

[3] A. K. Singh and Paras, "A dual-beam steering one-dimensional periodic leaky-wave antenna for large coverage," *AEÜ Int. J. Electron. Commun.*, vol. 145, p. 154086, 2022.

[4] R. Agarwal, R. L. Yadava, and S. Das, "A multilayered SIW-based circularly polarized CRLH leaky wave antenna," *IEEE Trans. Antennas Propag.*, vol. 69, no. 10, pp. 6312–6321, 2021.

[5] A. Sarkar, A. Sharma, and A. Biswas, "Compact CRLH leaky-wave antenna using TE_{20}-mode substrate-integrated waveguide for broad space radiation coverage," *IEEE Trans. Antennas Propag.*, vol. 68, no. 10, pp. 7202–7207, 2020.

[6] H. D. Li and L. Zhu, "Compact EH_0-mode microstrip leaky-wave antenna with enhanced gain in broadside," *IEEE Trans. Antennas Propag.*, vol. 70, no. 3, pp. 1837–1845, 2022.

[7] M. Wang, H. Ma, and W. Tang, "A dual-band electronic-scanning leaky-wave antenna based on a corrugated microstrip line," *IEEE Trans. Antennas Propag.*, vol. 67, no. 5, pp. 3433–3438, 2019.

[8] S. Ge, Q. Zhang, and C. Chiu, "Single-side-scanning surface waveguide leaky-wave antenna using spoof surface plasmon excitation," *IEEE Access*, vol. 6, pp. 66020–66029, 2018.

[9] S. Wang, K. Chung, and F. Kong, "A compact wide-angle frequency beam-scanning antenna using modulated composite waveguide based on half-mode substrate integrated waveguide and spoof surface plasmon polariton structure," *AEÜ Int. J. Electron. Commun.*, vol. 145, p. 154078, 2022.

[10] A. Aziz, "A novel plasmonic waveguide for extraordinary field enhancement of spoof surface plasmon polaritons with low-loss feature," *Results Opt.*, vol. 5, p. 100116, 2021.

[11] A. Moznebi, K. Afrooz, and A. Arsanjani, "Broadband bandpass filter and filtering power divider with enhanced slow-wave effect, compact size, and wide stopband based on butterfly-shaped spoof SPPs," *AEÜ Int. J. Electron. Commun.*, vol. 145, p. 154084, 2022.

[12] L. Liu, Y. Hu, and R. Li, "Compact and narrow-band bandpass filter using spoof surface plasmon polaritons," *IEEE Photon. Technol. Lett.*, vol. 33, no. 13, pp. 676–679, 2021.

[13] S. Zhu, P. Wen, and Y. Liu, "A compact filter based on spoof surface plasmon polariton waveguide for wide stopband suppression," *IEEE Photon. Technol. Lett.*, vol. 34, no. 9, pp. 475–478, 2022.

[14] B. Pan, P. Yu, and Z. Liao, "A compact filtering power divider based on spoof surface plasmon polaritons and substrate integrated waveguide," *IEEE Microw. Wirel. Compon. Lett.*, vol. 32, no. 2, pp. 101–104, 2022.

[15] X. Lv, W. Cao, and Z. Zeng, "A circularly polarized frequency beam scanning antenna (FBSA) fed by microstrip spoof SPP transmission line," *IEEE Antennas Wirel. Propag. Lett.*, vol. 17, no. 7, pp. 1329–1333, 2018.

[16] Q. Zhang, Q. Zhang, and Y. Chen, "High-efficiency circularly polarised leaky-wave antenna fed by spoof surface plasmon polaritons," *IET Microw. Antennas Propag.*, vol. 12, no. 10, pp. 1639–1644, 2018.

[17] H. Yu, Y. Jiao, and Z. Weng, "Spoof surface plasmon polariton-fed circularly polarized leaky-wave antenna with suppressed side-lobe levels," *Int. J. RF Microw. C. E.*, vol. 30, no. 3, pp. 1–9, 2020.

[18] K. Zhuang, J. Geng, and K. Wang, "Pattern reconfigurable antenna applying spoof surface plasmon polaritons for wide angle beam steering," *IEEE Access*, vol. 7, pp. 15444–15454, 2019.

[19] H. Zhang, T. Cui, and J. Xu, "Real-time controls of designer surface plasmon polaritons using programmable plasmonic metamaterial," *Adv. Mater. Technol.*, vol. 2, p. 1600202, 2016.

[20] A. Saghati, M. Mirsalehi, and M. Neshati, "A HMSIW circularly polarized leaky-wave antenna with backward, broadside, and forward radiation," *IEEE Antennas Wirel. Propag. Lett.*, vol. 13, pp. 451–454, 2014.

[21] Y. Lyu, F. Meng, and G. Yang, "Periodic SIW leaky-wave antenna with large circularly polarized beam scanning range," *IEEE Antennas Wirel. Propag. Lett.*, vol. 16, pp. 2493–2496, 2017.

[22] S. Chen, D. Karmokar, Z. Li, et al., "Circular-polarized substrate-integrated-waveguide leaky-wave antenna with wide-angle and consistent-gain continuous beam scanning," *IEEE Trans. Antennas Propag.*, vol. 67, no. 7, pp. 4418–4428, 2019.

[23] D. Liao, Y. Zhang, and H. Wang, "Wide-angle frequency-controlled beam-scanning antenna fed by standing wave based on the cutoff characteristics of spoof surface plasmon polaritons," *IEEE Antennas Wirel. Propag. Lett.*, vol. 17, no. 7, pp. 1238–1241, 2018.

[24] L. Jidi, X. Cao, and X. Zhu, "Printed frequency scanning antenna array with wide scanning angle range," *Prog. Electromagn. Res. Lett.*, vol. 77, pp. 117–122, 2018.

[25] T. Sabapathy, M. Jusoh, and R. B. Ahmad, "Wide angle scanning reconfigurable beam steering antenna," in *Proc. 2015 European Microw. Conf. (EuMC)*, IEEE, 2015, pp. 429–432.
[26] J. Yin, J. Ren, and Q. Zhang, "Frequency-controlled broad-angle beam scanning of patch array fed by spoof surface plasmon polaritons," *IEEE Trans. Antennas Propag.*, vol. 64, no. 12, pp. 5181–5189, 2016.
[27] R. Mani and M. Karthikeyan, "Full space scanning leaky wave antenna with wide angle beam steering based on SSPPs," *Eng. Res. Express*, 2025.
[28] R. Mani and M. Karthikeyan, "Wideband beam steering from backfire to end-fire miniaturized leaky wave antenna with PAM-shaped SSPP structure," *Phys. Scr.*, 2025.
[29] Y. Cheng, W. Hong, and K. Wu, "Millimeter-wave substrate integrated waveguide long slot leaky-wave antennas and two-dimensional multi-beam applications," *IEEE Trans. Antennas Propag.*, vol. 59, no. 1, pp. 40–47, 2011.
[30] T. Geibig, A. Shoykhetbrod, and A. Hommes, "Compact 3D imaging radar based on FMCW driven frequency-scanning antennas," in *Proc. 2016 IEEE Radar Conf.*, IEEE, 2016, pp. 1–5.
[31] S. T. Yang and H. Ling, "Range-azimuth tracking of humans using a microstrip leaky wave antenna," in *Proc. 2012 IEEE Int. Symp. Antennas Propag.*, IEEE, 2012, pp. 1–2.